

High- and low-cycle fatigue crack initiation using polycrystal plasticity

BY A. MANONUKUL† AND F. P. E. DUNNE

*Department of Engineering Science, University of Oxford,
Parks Road, Oxford OX1 3PJ, UK* (fionn.dunne@eng.ox.ac.uk)

Received 2 July 2003; accepted 23 September 2003; published online 8 April 2004

A polycrystal plasticity finite-element model has been developed for nickel-base alloy C263. That is, a representative region of the material, containing about 60 grains, has been modelled using crystal plasticity, taking account of grain morphology and crystallographic orientation. With just a single material property (in addition to standard elastic properties), namely, the critical resolved shear stress, the model is shown to be capable of predicting correctly a wide range of cyclic plasticity behaviour in face-centred cubic nickel alloy C263.

A fatigue crack initiation criterion is proposed, based simply on a critical accumulated slip. When this critical slip is achieved within the microstructure, crack initiation is taken to have occurred. The model predicts the development of persistent slip bands within individual grains with a width of *ca.* 10 µm. The model also predicts that crack initiation can occur preferentially at grain triple points under both low-(LCF) and high-cycle fatigue (HCF). For the case of HCF, this also corresponds to a free surface.

The polycrystal plasticity model combined with the fatigue crack initiation criterion are shown to predict correctly the standard Basquin and Goodman correlations in HCF, and the Coffin–Manson correlation in LCF. The model predictions are based on just two material properties: the critical resolved shear stress and the critical accumulated slip. Just one experimental test is required to determine these properties, for a given temperature, which have been obtained for nickel alloy C263. Predictions of life for nickel alloy C263 are then made over a broad range of loading conditions covering both LCF and HCF. Good agreement with experiments is achieved, despite the simplicity of the proposed ‘two-parameter’ model. A simple three-dimensional form of the model has provided an estimate of the fatigue limit for HCF crack initiation in C263.

Keywords: high-cycle fatigue (HCF); low-cycle fatigue (LCF);
crack initiation; polycrystal plasticity

1. Introduction

This paper addresses fatigue crack *initiation* in polycrystalline metals. In materials for which the lifetime under cyclic loading is dominated by crack initiation, the

† Present address: National Metal and Materials Technology Center, 73/1 Rama VI Road, Rajdhevee, Bangkok 10400, Thailand.

number of loading cycles required to cause a nucleated crack to propagate through the material to macroscopic failure is small compared with the number required to initiate the crack. This is initiation-controlled failure. We address both high- and low-cycle fatigue (HCF and LCF, respectively); that is, cyclic loading which leads to macroscopically purely elastic deformation (though full account of localized plasticity will be taken) and macroscopically plastic deformation, respectively. The approach used is to model the material using polycrystal plasticity theory, and to introduce a criterion for crack initiation. The model developed, which is based on just two material properties—the critical resolved shear stress and the critical accumulated plastic slip—is then tested against well-established HCF and LCF behaviour. In particular, HCF and LCF crack initiation in nickel-base alloy C263 are investigated using the model, and the results are tested against experimental data.

HCF and LCF have been under investigation for many years. HCF life is often determined empirically using Basquin's rule (Hertzberg 1983), and the effects of mean stress in HCF accounted for by using the Goodman rule (Hertzberg 1983). Similarly, LCF life can often be determined using the Manson–Coffin relationship (Manson & Hirschberg 1964). These empirical approaches can provide estimates of lifetime, usually only under simple, uniaxial loading conditions. The material parameters involved need to be determined for each material and usually for the particular loading conditions; that is, they often depend on temperature and stress range. They provide no insight into the crack initiation process and can only be used for extrapolation with great care. In general, these approaches include contributions from both the crack initiation phase, and the propagation phase; the two phases are not differentiated. In some materials, however, the number of cycles to initiate a fatigue crack dominates over the number for crack propagation. Initiation is, in any case, important regardless of whether it dominates fatigue life.

The mechanisms of fatigue crack initiation are often described in terms of the development of regions of persistent slip. In LCF, bulk plastic deformation takes place, but this is by no means homogeneous. In single phase polycrystalline metals with random crystallographic orientations, inhomogeneous stress and plastic strain fields are established because of orientation, grain shape and size, and geometrical effects (e.g. surfaces). It is expected, therefore, that localized regions of preferential slip develop, leading to similarly localized regions of crack initiation. In HCF, the material undergoes elastic deformation at the macroscopic level, and it is only in small areas (e.g. near a stress concentration at a free surface) that plastic deformation occurs, if at all. For the case of a polycrystalline metal subjected to HCF with uniform macroscopic stress, the localized regions deforming plastically are generated again by the inhomogeneity of the stress resulting from crystallographic orientation, grain shape, etc. Even in HCF, as very localized plastic straining develops, hardening can occur, leading to a redistribution of stress and a further localization of plasticity. In other words, this is shakedown occurring, and it is the basis of the Dang Van criterion for crack initiation (Dang Van 1993; Ballard *et al.* 1995; Peridas & Hills 2002). Dang Van argues that local plastic flow is essential for crack initiation and that, were shakedown to occur, at the grain level, the material would have an infinite fatigue life. While this may be close to the truth, there are arguments that crack initiation in HCF can occur even if the critical resolved shear stress within an individual grain is never exceeded. However, it is accepted that irreversible dislocation motion is, nonetheless, required. In any case, the difficulty comes, when using Dang Van's

model, in relating the macroscopic stress state to that which exists at the grain level. The difficulty is side-stepped by Dang Van's approach, which then becomes similar in many ways to the traditional macro-level correlations. However, Dang Van's method is an attempt to provide a more fundamental approach to quantifying fatigue crack initiation.

In the present work, by considering only a representative volume of a material, polycrystal plasticity theory is used to model the details of grain morphology and crystallographic orientation (Harder 1999; Toth *et al.* 2000; Saanouni & Abdul-Latif 1996; Dingli *et al.* 2000). In this way, the relationship between the macroscopic stress state and that which exists at the grain level can be investigated in detail. In addition, it enables the determination of the inhomogeneous fields of plastic strain, the identification of regions of localized plasticity (persistent slip bands) and grain-level shakedown. While it is not discussed in this paper, it provides a method by which the Dang Van 'localization tensor' may be obtained. In this paper, a fatigue crack initiation criterion is presented, and combined with the polycrystal plasticity model to provide a fundamental approach for the determination of fatigue crack initiation in HCF and LCF. The majority of the modelling is carried out in two dimensions. Three-dimensional models are developed for consideration of crack initiation in HCF. In the following section, the crystal plasticity model and its application to nickel-base alloy C263 is described.

2. Crystal plasticity model

Rate effects are not considered in the present investigation and, for this reason, a time-independent plasticity model is adopted. It is based on that developed by Asaro (1983) and Anand & Kothari (1996). When a load is applied, the total deformation and rotation of a crystal is given by the deformation gradient \mathbf{F} , which can be written in terms of elastic and plastic parts

$$\mathbf{F} = \mathbf{F}^e \mathbf{F}^p. \quad (2.1)$$

The material undergoes plastic slip, γ , through the 'undeformed' crystal lattice given by

$$\mathbf{F}^p = \mathbf{I} + (\mathbf{s}^\alpha \mathbf{n}^{\alpha T}) \gamma^\alpha. \quad (2.2)$$

In addition, the crystal lattice and material undergo rigid body rotation and elastic deformation given by \mathbf{F}^e .

Unit vectors that represent the initial slip on the α th slip system within the crystal lattice (with slip direction \mathbf{s}_0^α and normal \mathbf{n}_0^α) will deform and rotate as a result of the 'elastic' deformation gradient \mathbf{F}^e . Note that \mathbf{F}^e here includes both the conventional elastic deformation and the rigid body rotation. Hence,

$$\mathbf{s}^\alpha = \mathbf{F}^e \mathbf{s}_0^\alpha, \quad \mathbf{n}^\alpha = (\mathbf{F}^e)^{-1} \mathbf{n}_0^\alpha \quad \text{and} \quad \mathbf{s}_0^\alpha \cdot \mathbf{n}_0^\alpha = \mathbf{s}^\alpha \cdot \mathbf{n}^\alpha = 0. \quad (2.3)$$

In general, \mathbf{s}^α and \mathbf{n}^α are not unit vectors, but always remain perpendicular.

A pseudo-time-scale can be introduced so that the velocity gradient in the current configuration is given by

$$\mathbf{L} = \dot{\mathbf{F}} \mathbf{F}^{-1} = \dot{\mathbf{F}}^e (\mathbf{F}^e)^{-1} + \mathbf{F}^e \dot{\mathbf{F}}^p (\mathbf{F}^p)^{-1} (\mathbf{F}^e)^{-1}. \quad (2.4)$$

The velocity gradient \mathbf{L} can also be decomposed into the deformation rate \mathbf{D} and the spin tensor \mathbf{W}

$$\mathbf{L} = \mathbf{D} + \mathbf{W}, \quad (2.5)$$

where

$$\left. \begin{aligned} \mathbf{D} &= \frac{1}{2}(\mathbf{L} + \mathbf{L}^T), & \mathbf{W} &= \frac{1}{2}(\mathbf{L} - \mathbf{L}^T), & \mathbf{D} &= \mathbf{D}^e + \mathbf{D}^p, \\ \mathbf{W} &= \mathbf{W}^e + \mathbf{W}^p, & \mathbf{L} &= \mathbf{L}^e + \mathbf{L}^p. \end{aligned} \right\} \quad (2.6)$$

In addition, the plastic velocity gradient can also be defined as the sum of the shearing rates, $\dot{\gamma}^\alpha$ on all the slip systems due to dislocation slip (Asaro 1983):

$$\mathbf{L}^p = \sum_{\alpha=1}^n \dot{\gamma}^\alpha \mathbf{s}^\alpha \mathbf{n}^{\alpha T}. \quad (2.7)$$

The plastic deformation rate \mathbf{D}^p and the plastic spin tensor \mathbf{W}^p can also be derived from the symmetric and skew parts, respectively, of the plastic velocity gradient \mathbf{L}^p as

$$\mathbf{D}^p = \sum_{\alpha=1}^n \mathbf{P}^\alpha \dot{\gamma}^\alpha \quad (2.8)$$

and

$$\mathbf{W}^p = \sum_{\alpha=1}^n \boldsymbol{\Omega}^\alpha \dot{\gamma}^\alpha, \quad (2.9)$$

where

$$\mathbf{P}^\alpha = \frac{1}{2}(\mathbf{s}^\alpha \mathbf{n}^{\alpha T} + \mathbf{n}^\alpha \mathbf{s}^{\alpha T}) \quad (2.10)$$

and

$$\boldsymbol{\Omega}^\alpha = \frac{1}{2}(\mathbf{s}^\alpha \mathbf{n}^{\alpha T} - \mathbf{n}^\alpha \mathbf{s}^{\alpha T}). \quad (2.11)$$

Combining equations (2.6), (2.8) and (2.9), the elastic deformation rate and elastic spin tensor are

$$\mathbf{D}^e = \mathbf{D} - \sum_{\alpha=1}^n \mathbf{P}^\alpha \dot{\gamma}^\alpha \quad (2.12)$$

and

$$\mathbf{W}^e = \mathbf{W} - \sum_{\alpha=1}^n \boldsymbol{\Omega}^\alpha \dot{\gamma}^\alpha. \quad (2.13)$$

The elastic law for crystals under large deformation (Hill & Rice 1972) is

$$\bar{\boldsymbol{\sigma}} + \boldsymbol{\sigma} \operatorname{tr}(\mathbf{D}^e) = \mathbf{C} : \mathbf{D}^e, \quad (2.14)$$

where \mathbf{C} is the elastic modulus and a fourth-order tensor, and $\bar{\boldsymbol{\sigma}}$ is the Jaumann rate of Cauchy stress based on the axes that spin together with the lattice, which is given in terms of Cauchy stress rate $\dot{\boldsymbol{\sigma}}$ by

$$\bar{\boldsymbol{\sigma}} = \dot{\boldsymbol{\sigma}} - \mathbf{W}^e \boldsymbol{\sigma} + \boldsymbol{\sigma} \mathbf{W}^e. \quad (2.15)$$

Substituting equation (2.12) into (2.14), the Jaumann stress rate can be written as

$$\bar{\dot{\sigma}} = \mathbf{C} : \mathbf{D} - \mathbf{C} : \sum_{\alpha=1}^n \mathbf{P}^\alpha \dot{\gamma}^\alpha - \boldsymbol{\sigma} \operatorname{tr}(\mathbf{D}^e). \quad (2.16)$$

Since

$$\operatorname{tr}(\mathbf{D}^p) = 0 \quad \text{and} \quad \operatorname{tr}(\mathbf{D}) = \operatorname{tr}(\mathbf{D}^e), \quad (2.17)$$

equation (2.16) can also be written as

$$\dot{\sigma} = \mathbf{C} : \mathbf{D} - \mathbf{C} : \sum_{\alpha=1}^n \mathbf{P}^\alpha \dot{\gamma}^\alpha - \boldsymbol{\sigma} \operatorname{tr}(\mathbf{D}). \quad (2.18)$$

From equations (2.15) and (2.18), the Cauchy stress rate is given by

$$\dot{\sigma} = \mathbf{C} : \mathbf{D} - \mathbf{C} : \sum_{\alpha=1}^n \mathbf{P}^\alpha \dot{\gamma}^\alpha - \boldsymbol{\sigma} \operatorname{tr}(\mathbf{D}) + \mathbf{W}^e \boldsymbol{\sigma} - \boldsymbol{\sigma} \mathbf{W}^e. \quad (2.19)$$

Using equation (2.13), the Cauchy stress rate can be expressed in terms of the total quantity \mathbf{W} as

$$\dot{\sigma} = \mathbf{C} : \mathbf{D} - \mathbf{C} : \sum_{\alpha=1}^n \mathbf{P}^\alpha \dot{\gamma}^\alpha - \boldsymbol{\sigma} \operatorname{tr}(\mathbf{D}) + \left(\mathbf{W} - \sum_{\alpha=1}^n \boldsymbol{\Omega}^\alpha \dot{\gamma}^\alpha \right) \boldsymbol{\sigma} - \boldsymbol{\sigma} \left(\mathbf{W} - \sum_{\alpha=1}^n \boldsymbol{\Omega}^\alpha \dot{\gamma}^\alpha \right), \quad (2.20)$$

and rearranged to give

$$\dot{\sigma} = \mathbf{C} : \mathbf{D} - \boldsymbol{\sigma} \operatorname{tr}(\mathbf{D}) - \mathbf{W} \boldsymbol{\sigma} + \boldsymbol{\sigma} \mathbf{W} - \sum_{\alpha=1}^n (\mathbf{C} : \mathbf{P}^\alpha + \boldsymbol{\beta}^\alpha) \dot{\gamma}^\alpha, \quad (2.21)$$

where

$$\boldsymbol{\beta}^\alpha = \boldsymbol{\Omega}^\alpha \boldsymbol{\sigma} - \boldsymbol{\sigma} \boldsymbol{\Omega}^\alpha. \quad (2.22)$$

In order to obtain the Cauchy stress rate, it is necessary to determine the shearing rate $\dot{\gamma}^\alpha$ on the α th active slip system. The conditions under which a slip system is active or inactive are based on the yield and loading-unloading criteria. The magnitude of $\dot{\gamma}^\alpha$ can be determined using the constitutive equation for plastic slip on each slip system,

$$\dot{\tau}_c^\alpha = \sum_{\alpha=1}^n \mathbf{h}^{\alpha\beta} \dot{\gamma}^\alpha, \quad (2.23)$$

where τ_c^α is the current critical resolved shear stress and $\mathbf{h}^{\alpha\beta}$ is the hardening modulus matrix. The modulus $h^{\alpha\beta}$ describes the hardening on slip system α due to shearing on slip system β . Modulus $h^{\alpha\alpha}$ represents the self-hardening effect and modulus $h^{\alpha\beta}$ ($\alpha \neq \beta$) represents the latent-hardening effect. Note that the hardening modulus matrix is the least well-characterized part of the constitutive equation for crystal elasto-plasticity (Anand & Kothari 1996). There are 144 moduli in a face-centred cubic (FCC) crystal to be specified.

An α th slip system is considered to slip, or flow plastically, when the resolved shear stress on the slip system τ^α exceeds a critical resolved shear stress τ_c^α . The critical resolved shear stress τ_c^α is determined by the current dislocation density

and substructure. The planes $\tau^\alpha = \tau_c^\alpha$ represent the facets of the current pyramidal yield surface in stress space. The outward unit normal to the yield facets is \mathbf{P}^α . A slip system is considered inactive if $\tau^\alpha < \tau_c^\alpha$, or $\tau^\alpha = \tau_c^\alpha$ and a trial stress rate $\mathbf{P}^\alpha : \mathbf{C} : \mathbf{D}$ points inside the yield surface, i.e. the system is under an unloading condition. On the other hand, a slip system is considered active if $\tau^\alpha = \tau_c^\alpha$ and a trial stress rate $\mathbf{P}^\alpha : \mathbf{C} : \mathbf{D}$ points outside the yield surface, i.e. the system is under a loading condition:

$$\left. \begin{array}{ll} \dot{\gamma}^\alpha = 0, & \text{if } \tau^\alpha < \tau_c^\alpha, \\ \dot{\gamma}^\alpha = 0, & \text{if } \tau^\alpha = \tau_c^\alpha \text{ and } \mathbf{P}^\alpha : \mathbf{C} : \mathbf{D} \leq 0, \\ \dot{\gamma}^\alpha \geq 0, & \text{if } \tau^\alpha = \tau_c^\alpha \text{ and } \mathbf{P}^\alpha : \mathbf{C} : \mathbf{D} > 0. \end{array} \right\} \quad (2.24)$$

The resolved shear stress, or Schmid stress, on the α th slip system is defined as (Asaro & Rice 1977)

$$\tau^\alpha = \mathbf{s}^\alpha(\boldsymbol{\sigma} n^\alpha) = \mathbf{P}^\alpha : \boldsymbol{\sigma}. \quad (2.25)$$

The rate of change of the resolved shear stress on the α th slip system can be obtained by taking the material time derivative of equation (2.25),

$$\dot{\tau}^\alpha = \mathbf{P}^\alpha : \dot{\boldsymbol{\sigma}} + \dot{\mathbf{P}}^\alpha : \boldsymbol{\sigma}, \quad (2.26)$$

where the superscript ‘ ∇ ’ indicates a co-rotational rate.

Note that it is possible to prove that (Asaro 1983)

$$\dot{\mathbf{P}}^\alpha : \boldsymbol{\sigma} = \boldsymbol{\beta}^\alpha : \mathbf{D}^e. \quad (2.27)$$

Substituting equation (2.12) into equation (2.27)

$$\mathbf{P}^\alpha : \dot{\boldsymbol{\sigma}} = \boldsymbol{\beta}^\alpha : \left(\mathbf{D} - \sum_{\alpha=1}^n \mathbf{P}^\alpha \dot{\gamma}^\alpha \right). \quad (2.28)$$

Combining equations (2.18), (2.26) and (2.28), the rate of change of the resolved shear stress is given by

$$\dot{\tau}^\alpha = \mathbf{P}^\alpha : \left(\mathbf{C} : \mathbf{D} - \mathbf{C} : \sum_{\alpha=1}^n \mathbf{P}^\alpha \dot{\gamma}^\alpha - \boldsymbol{\sigma} \operatorname{tr}(\mathbf{D}) \right) + \boldsymbol{\beta}^\alpha : \left(\mathbf{D} - \sum_{\alpha=1}^n \mathbf{P}^\alpha \dot{\gamma}^\alpha \right). \quad (2.29)$$

To satisfy the consistency condition during plastic slip,

$$\dot{\tau}^\alpha = \dot{\tau}_c^\alpha, \quad (2.30)$$

and hence, from equations (2.23) and (2.29),

$$\sum_{\alpha=1}^n \mathbf{h}^{\alpha\beta} \dot{\gamma}^\alpha = \mathbf{P}^\alpha : \left(\mathbf{C} : \mathbf{D} - \mathbf{C} : \sum_{\alpha=1}^n \mathbf{P}^\alpha \dot{\gamma}^\alpha - \boldsymbol{\sigma} \operatorname{tr}(\mathbf{D}) \right) + \boldsymbol{\beta}^\alpha : \left(\mathbf{D} - \sum_{\alpha=1}^n \mathbf{P}^\alpha \dot{\gamma}^\alpha \right). \quad (2.31)$$

Rewriting the above equation gives

$$\sum_{\alpha=1}^n \mathbf{A}^{\alpha\beta} \dot{\gamma}^\alpha = b^\alpha, \quad (2.32)$$

where

$$\mathbf{A}^{\alpha\beta} = \mathbf{h}^{\alpha\beta} + \mathbf{P}^\alpha : \mathbf{C} : \mathbf{P}^\alpha + \boldsymbol{\beta}^\alpha : \mathbf{P}^\alpha, \quad (2.33)$$

and

$$b^\alpha = \mathbf{P}^\alpha : [\mathbf{C} : \mathbf{D} - \boldsymbol{\sigma} \operatorname{tr}(\mathbf{D})] + \boldsymbol{\beta}^\alpha : \mathbf{D}. \quad (2.34)$$

Equation (2.32) contains a set of linear equations. When the matrix $\mathbf{A}^{\alpha\beta}$ is singular, equation (2.32) has a solution but it is non-unique. This is a well-known problem with time-independent crystal plasticity, which results from the non-uniqueness of the solutions for $\dot{\gamma}^\alpha$ when more than five slip systems are active at the same time (Khan & Huang 1995). Anand & Kothari (1996) overcome this problem by using a singular-value decomposition to obtain a pseudo-inverse of a singular (or very close to singular) matrix (Golub & van Loan 1983; Press *et al.* 1986; Strang 1988), and this is adopted here.

(a) Material parameters

Nickel-base superalloy C236 has an FCC crystal structure, which has 12 $\{111\}\langle110\rangle$ octahedral slip systems. The crystal plasticity constitutive model for an FCC crystal requires the initial critical resolved shear stress for each slip system τ_c^α and the hardening modulus matrix $\mathbf{h}^{\alpha\beta}$ to be identified. There are many forms suggested for the hardening modulus matrix. Here we have taken one of the simple forms suggested by Peirce *et al.* (1982),

$$\mathbf{h}^{\alpha\beta} = \begin{pmatrix} h & qh & \cdots & \cdots \\ qh & h & qh & \cdots \\ \cdots & qh & h & qh \\ \cdots & \cdots & qh & h \end{pmatrix}, \quad (2.35)$$

where h is a self-hardening rate and q is the latent-hardening ratio. Taylor & Elam (1925) conclude that slip systems are hardened by slip on other systems and the latent hardening rate is at least comparable in magnitude or higher than the self-hardening rate. Hence, $q \geq 1$.

Thus, we have three plasticity parameters to be determined: the initial critical resolved shear stress τ_c , the self-hardening rate h and the latent-hardening ratio q . In addition, the elastic modulus matrix is required.

(b) Polycrystal plasticity finite-element modelling of nickel-base alloy C236

Figure 1a shows a typical microstructure of the standard heat-treated nickel-base alloy C236. This is an FCC material with grains having a nominally random crystallographic orientation. After standard heat treatment at 1150 °C for 2 h, quenching in water and ageing at 800 °C for 8 h followed by air cooling, the material has a mean grain size of 104 µm and a 9.5% volume fraction of Ni₃(Ti,Al) γ' precipitate with an average size of 22 nm, and an almost continuous precipitation of M₂₃C₆ carbide at grain boundaries. The γ' precipitates are negligibly small compared with the grain size, and are uniformly distributed throughout the grains (Manonukul *et al.* 2002). Because of their size, it is argued that their effect on the local stress fields within

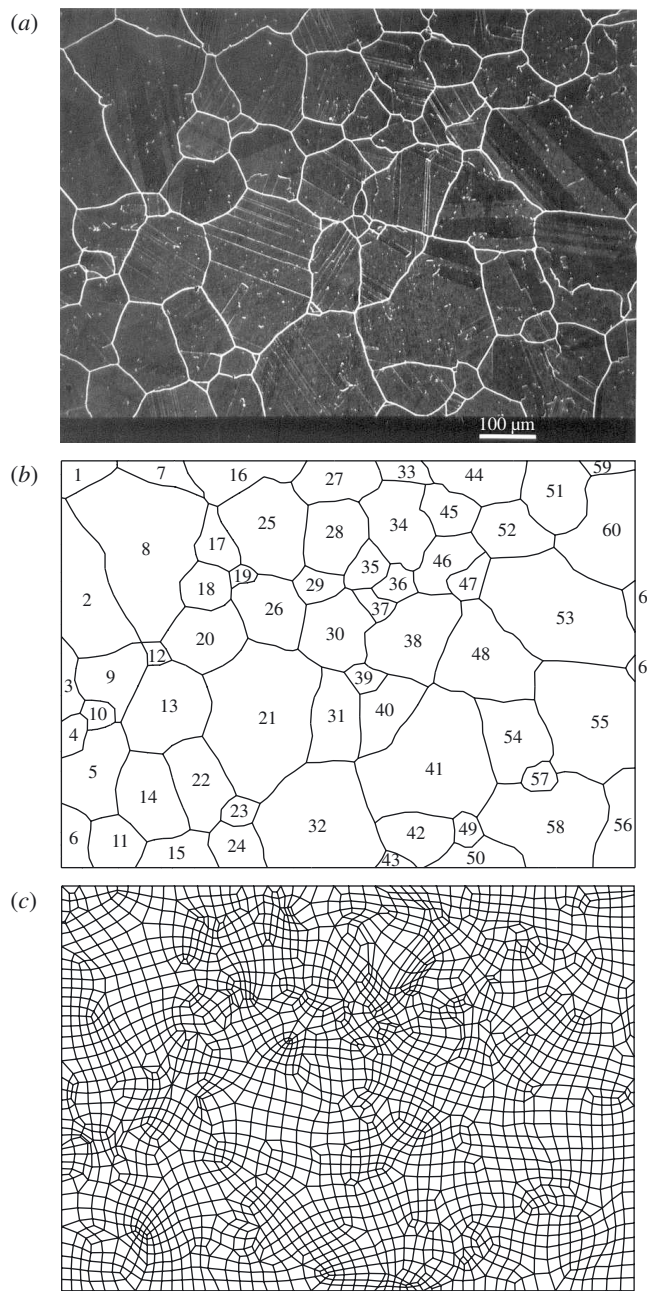


Figure 1. (a) A typical microstructure of the standard heat-treated C263; (b) the grain boundaries simulated; (c) a finite-element mesh for the corresponding microstructure.

the grains is at a length-scale too small to influence grain-level stress and strain inhomogeneity. They have not, therefore, been modelled explicitly.

The material's grain boundaries have been identified as shown in figure 1b. Each grain has been meshed initially using four-noded plane-strain elements as shown

in figure 1c. For the majority of the calculations reported here, three-dimensional elements are not used because of the computational expense. Plane-stress elements have not been used because of the need to calculate macro-level stresses from the finite-element representation of the microstructure. This will become apparent later. However, the use of plane-strain elements to simulate uniaxial loading does mean that a plane-strain-compensated elastic modulus ($E[1 - \nu^2]$) had to be used in the calculations, when comparisons were made with nominally plane-stress experimental results. The effects of this will be addressed later.

In the model, there are 62 grains and 2313 elements in total. The free edges were constrained to remain straight, in order to represent a repeating unit of this typical microstructure. This is an important point, in that we are not, here, trying to represent a real component (e.g. a test specimen) with all that that implies in terms of geometry and free surfaces. Under HCF conditions, in particular, free surfaces are often found to be the locations of fatigue crack initiation, because, it is argued, the free surface together with the local inhomogeneity produced by grains with different shapes and crystallographic orientations lead to conditions conducive to generating accumulated plastic slip. Initially, we consider a simpler problem: given a representative cell of a material's microstructure, how do crystallographic orientation and grain morphology influence the accumulation of plastic slip? Later in the paper, the importance of this will be addressed in the context of the critical accumulated plastic slip required for crack initiation. For HCF in particular, three-dimensional models with free surfaces are also considered.

In figure 1c, the left and bottom free edges are axes of symmetry. Under strain-controlled fatigue simulation, the loading is applied using a displacement subroutine to specify the displacement on the top free edge. Under stress control, a uniformly distributed load is applied at the top free edge. The crystal plasticity constitutive equations were implemented into a user-defined material subroutine within the ABAQUS nonlinear finite-element solver. Random crystallographic orientations for each grain were generated. All finite elements falling within a grain were therefore allocated the crystallographic orientation corresponding to that grain. The models were run on a Cray Origin 2000 parallel computer. This consists of 96 central processing units (CPUs) with 195 MHz R10000 processors, each with 256 Mb of RAM (total shared memory of 24 Gb). A typical computer run time for two LCF cycles is 20 h using 2 CPUs.

LCF tests have been carried out by Zhang & Knowles (2002) on C263 at 20 and 600 °C for fully reversed strain-controlled loading with zero mean strain (R ratio = -1 , that is, the ratio of the minimum to the maximum stress in a cycle), and by DERA at 300 °C for strain control with different mean strains (R ratio = 0 and R ratio = -1). HCF tests have been carried out by Rolls-Royce on C263 at 20 °C. Note that the HCF results were determined from rotating-bend tests.

The experimental saturated LCF stress-strain hysteresis loops at 20 °C have been used to determine the plasticity material properties. Fully reversed, strain-controlled, uniaxial tests with R ratio = -1 at strain amplitudes ± 1.0 , 0.5 and 0.37% were carried out, and the experimental saturated stress-strain loops are shown by the broken lines in figure 2. The same strain-controlled loading was applied to the finite-element model shown in figure 1c. The resulting macro-level stress is calculated, at any time, by summing the nodal reaction forces on the top edge and dividing by the current cross-sectional area. The solid lines show the computed results, which saturate after

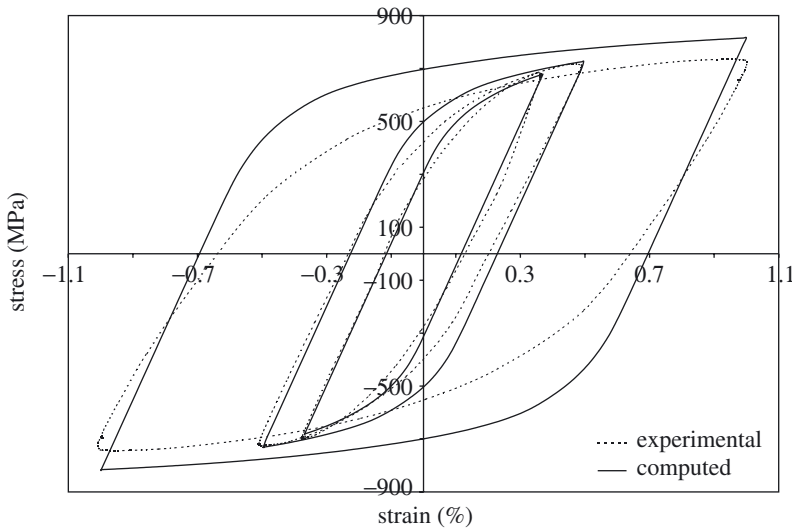


Figure 2. Comparison between experimental and computed stress–strain curves for LCF at 20 °C for the strain amplitudes 0.37, 0.5 and 1.0%.

just two cycles. For the computed data, the elastic modulus, the hardening constants and the material's critical resolved shear stress have been obtained to ensure the best representation of the experimental data at a strain range of 0.5% (Poisson's ratio is taken as 0.3 throughout). In fact, this requires the self-hardening and latent-hardening parameters, h and q , to be set to zero. The hardening that appears in the computed stress–strain loops comes solely from the inhomogeneous stress fields established because of the random orientation of the grains. Yielding is therefore highly localized and progressive and, for an individual grain, depends upon the local slip direction and how quickly the resolved shear stress achieves its critical value. The calculated hysteresis loops shown in figure 2 were therefore obtained using only the material's elastic properties (which are assumed here to be isotropic) and the material's critical resolved shear stress. Given this, the agreement with the experiments over the range of strain amplitudes considered is good.

For the particular case of the 0.5% strain range, the experimental and computed results are shown in figure 3. In addition, the calculations have been repeated for a different set of randomly generated grain orientations, and these results are superimposed in figure 3. The two different sets of orientations generate nearly identical results, indicating that a sufficiently large number of differently orientated grains has been included in the model, and that at the macro-level the model representing the microstructure will be isotropic in both elasticity and plasticity, and will reproduce the results of J_2 (that is, conventional von Mises continuum) flow theory.

A similar process to that used for 20 °C was carried out for temperatures of 300 and 600 °C, and the material properties are summarized in table 1.

The critical resolved shear stresses given in table 1 appear to be high, at least compared with those for pure nickel. However, it should be noted that the values obtained here correspond to those for the material in the cyclically hardened state, so that considerably higher values than those for the virgin material would be expected.

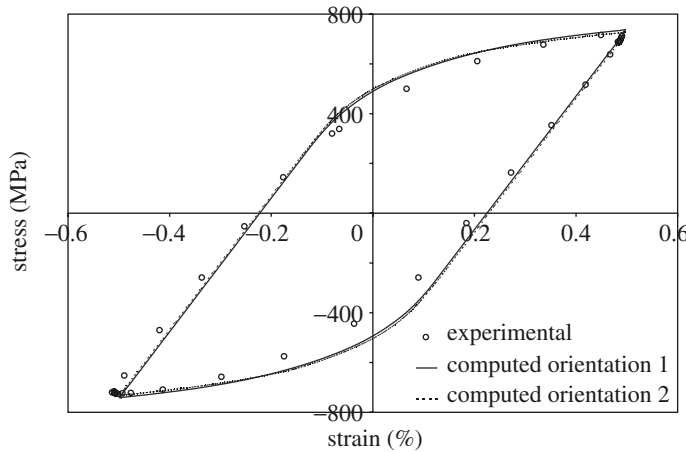


Figure 3. Predicted stress-strain curves for different initial crystallographic orientations for LCF at 20 °C, and experimental data for the same loading conditions.

Table 1. Temperature dependence of Young's modulus and critical resolved shear stress

temperature (°C)	(plane-strain compensated) elastic modulus (GPa)	critical resolved shear stress (MPa)
20	244	230
300	193	225
600	178	205

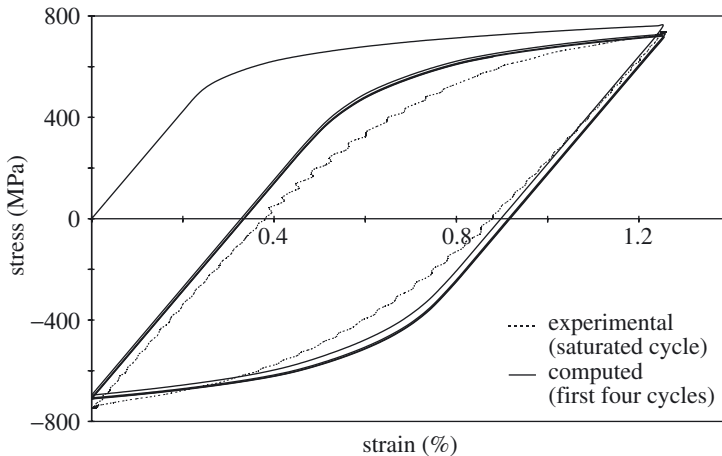


Figure 4. Comparison between experimental (saturated cycle only) and computed (first four cycles) stress-strain curves for LCF at 300 °C, R ratio = 0.

Good agreement between computed and experimental stress-strain behaviour is achieved for the three temperatures and for a range of strain amplitudes, using only the two material properties given for each temperature. Figure 4 shows the comparison between predicted and experimental stress-strain behaviour for LCF at

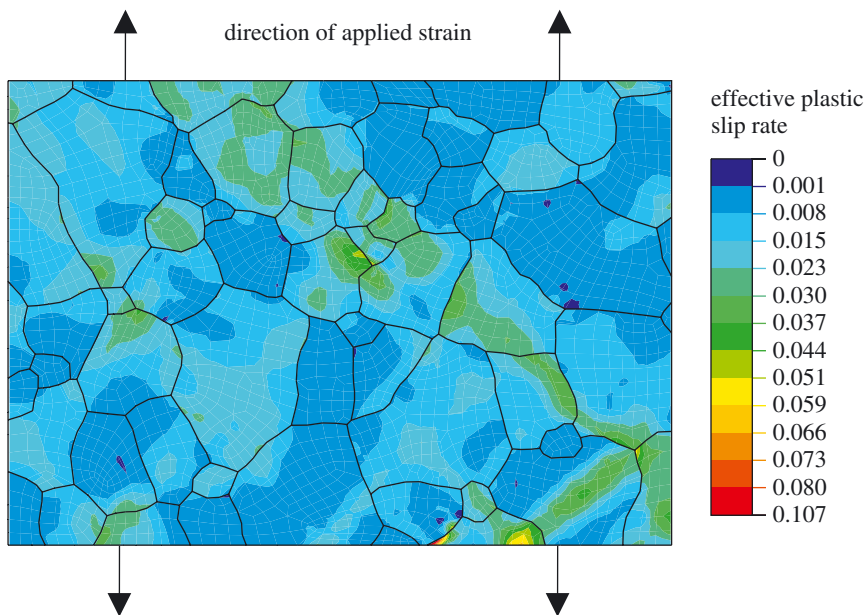


Figure 5. Field plot of effective plastic slip rate at the end of the second cycle in LCF at 300 °C, R ratio = 0.

300 °C with an R ratio = 0. A predicted stabilized loop is obtained after just a couple of cycles, which agrees well with the saturated experimental loop.

The plastic velocity gradient, \mathbf{L}^p , is defined by

$$\mathbf{L}^p = \sum_{\alpha=1}^n \dot{\gamma}^\alpha \mathbf{s}^\alpha \mathbf{n}^{\alpha T}. \quad (2.36)$$

An effective plastic slip rate, \dot{p} , is now introduced, and defined as

$$\dot{p} = (\frac{2}{3} \mathbf{L}^p : \mathbf{L}^p)^{1/2}. \quad (2.37)$$

Because in all the analyses carried out here the rigid body rotations are small, \dot{p} is, in effect, identical to the effective plastic slip rate. It is interesting to examine the distribution of the plastic slip rate throughout the deforming microstructure. This is shown for LCF at 300 °C, with an R ratio equal to zero, at the end of the second cycle in figure 5. It shows the localization of plastic slip both at a transgranular level, which indicates the formation of bands of plasticity at ca. 45° to the loading direction, and within individual grains. The latter results from the grain shape, the surrounding constraint and the grain crystallographic orientation. There are a few locations at which redistribution of stress has led to shakedown such that, at these locations, the deformation is purely elastic (and hence the effective plastic slip rate is zero).

3. Fatigue crack initiation in LCF and HCF

It is argued that the polycrystal plasticity model presented above enables the determination of stress and strain at the microstructural level. A fundamental quantity

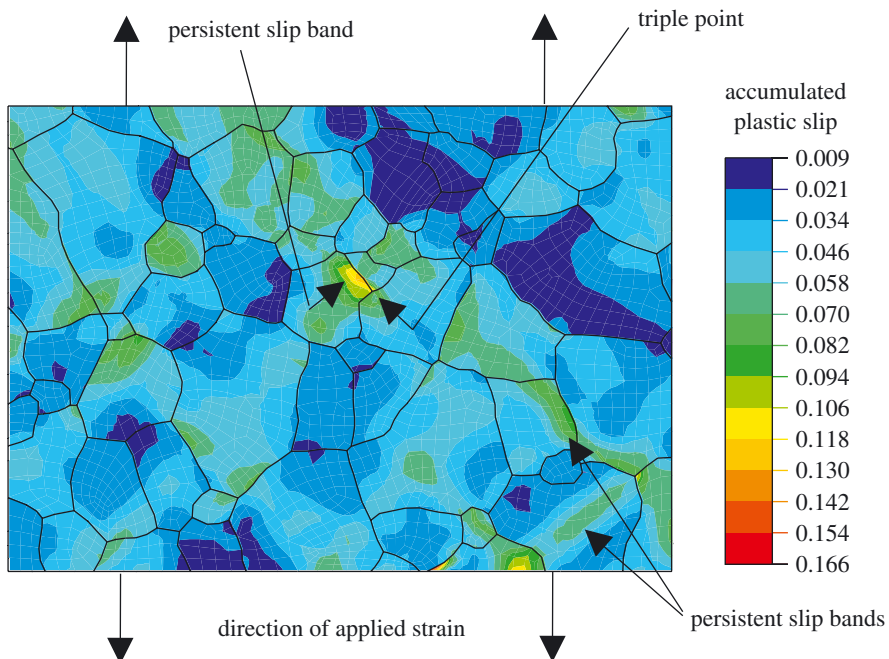


Figure 6. Field plot of accumulated plastic slip after two cycles of fully reversed LCF with strain amplitude of 0.5%.

at the micro-level must be the accumulated (plastic) slip, which, like strain, is a dimensionless quantity, and can be calculated for every point in the finite-element model as

$$p = \int_0^t \dot{p} dt. \quad (3.1)$$

Some authors (Skelton *et al.* 1998; A. Korsunsky 2002, personal communication) have argued that crack initiation, and indeed growth, should depend upon local energy dissipation. The crack initiation criterion adopted here is trivially simple, but based on local accumulated effective slip, p . However, it would be perfectly possible to use the methodology presented here to address the equivalence, or otherwise, of the energy approach. Because at the level of slip within grains the material behaves perfectly plastically (recall that the hardening parameters, q and h , are set to zero), it is argued that strain-based and energy-based fatigue crack initiation criteria are likely to lead to the same result, at least in the material considered in this paper. However, here a general initiation criterion is proposed, applicable to both HCF and LCF, based on (plastic) slip.

It is argued that there exists a critical accumulated slip, p_c , at the micro-level, which once achieved, leads to crack initiation. The accumulated slip, p , is calculated at all material points in the microstructure, and its values monitored. The criterion for initiation may be written

$$p = p_{\text{crit}}. \quad (3.2)$$

Figure 6 shows the field variation of p after two cycles of fully reversed LCF at 300 °C with strain amplitude 0.5%. It can be seen how localized this quantity is, with

the peak values occurring at just one or two grain boundaries. The higher values of accumulated slip in general follow the grain boundaries, but it can be seen that the highest values occur at, or close to, grain triple points. It can also be seen that the accumulated slip is localized even within individual grains, leading to the formation of intense bands of slip-persistent slip bands. These are often also associated with triple points. The average grain size is *ca.* 100 µm, so the width of the slip bands lies within the range 1–20 µm. Schwab *et al.* (1996) observed in experiments the formation of persistent slip bands in single crystals of nickel at 300 K with widths up to *ca.* 10 µm.

With the calculation of the maximum accumulated slip, together with knowledge of the experimentally determined number of cycles to failure, N_f , for a particular test with known loading conditions, it is in principle possible to determine the critical accumulated slip, p_{crit} . Because the stress-strain behaviour stabilizes very quickly (generally in less than two cycles), it is possible to calculate the accumulated slip per cycle, p_{cyc} . The crack initiation criterion may then be rewritten

$$p_{\text{cyc}}N_f = p_{\text{crit}}. \quad (3.3)$$

The critical accumulated slip, p_{crit} , should be a fundamental quantity. Provided the mechanisms of slip remain unaltered, that is, octahedral (as opposed to cubic), slip continues to dominate for FCC materials, and diffusion has negligible effect; once determined, it should be possible to predict the occurrence of crack initiation over a range of temperature and for both LCF and HCF.

It is important to note that the determination of the critical accumulated slip, p_{crit} , requires experimental knowledge of when crack *initiation* occurs. This is not always easy to determine. However, in general, it is easy to determine the number of cycles to *failure*. If, as is the case for the material considered here, the number of cycles to crack initiation is much larger than that for propagation, we can equate the critical accumulated slip (for crack *initiation*) with the accumulated slip to cause failure. Hence, in this way, we can determine p_{crit} from an experiment, because we know the number of cycles to failure, and we have calculated the slip per cycle, p_{cyc} . For initiation-dominated failure, this is reasonable. For propagation-controlled failure, clearly it is not reasonable, but this paper is concerned with crack initiation. Indeed, experimental evidence for C263 shows that initiation largely dominates the fatigue life unless the number of cycles to failure is small for LCF (S. Williams 2002, personal communication). Chan (2003) draws together the results of many fatigue experiments and shows that the number of cycles required to cause crack initiation is often a significant fraction of those required to cause failure, and that in some materials the initiation phase dominates the material's life. Wei *et al.* (1991) investigated LCF in nickel-base superalloy IN100 and show that, in this alloy also, initiation completely dominates life for strain amplitudes less than *ca.* 0.4%. Shepherd *et al.* (2001) discuss lifting methodologies for aero-engine materials, and in particular, nickel-base superalloys. They identify the importance of examining separately the contributions of the crack initiation and propagation phases leading to failure. We are concerned in this paper with $\log(\text{number of cycles to failure}) > 3.3$, and hence, our assumption of initiation-dominated lifetimes is reasonable. Reference should again, perhaps, be made to HCF, in which cracks often initiate at free surfaces. We have chosen a single LCF test to determine the critical accumulated slip and realize that, in making predictions for HCF, we should ideally be modelling explicitly the free

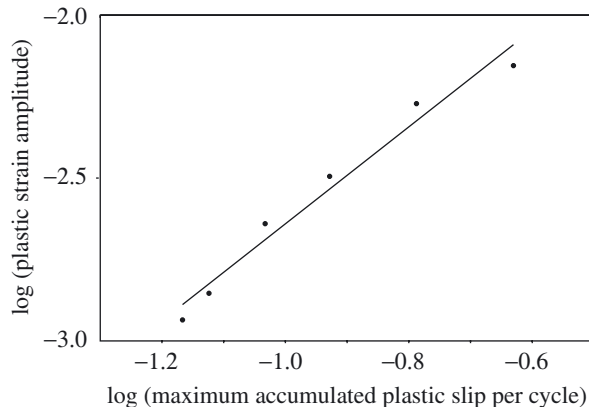


Figure 7. Predicted relationship between maximum accumulated plastic slip per cycle and plastic strain amplitude for LCF at 20 °C. The linear fit is included to indicate the trend.

surfaces. This is addressed later. LCF and HCF crack initiation are investigated in the following sections.

(a) LCF crack initiation

Before determining the critical accumulated slip for nickel-base alloy C263, LCF is considered more generally. Crack initiation (for initiation-controlled failure) in LCF is often correlated well with the Coffin–Manson relationship, namely

$$\Delta\varepsilon_p N_f^a = C_1, \quad (3.4)$$

in which $\Delta\varepsilon_p$ is the macroscale plastic strain range and C_1 and a are material constants. With the fatigue crack initiation criterion given in equation (3.3), this can be written as

$$\Delta\varepsilon_p \left(\frac{p_{\text{crit}}}{p_{\text{cyc}}} \right)^a = C_1, \quad (3.5)$$

or

$$\ln \Delta\varepsilon_p = \ln \beta + a \ln p_{\text{cyc}}, \quad (3.6)$$

in which β is just a constant, since p_{crit} is constant. The polycrystal finite-element model has been used to calculate the accumulated slip per cycle, p_{cyc} , for a range of applied macroscale strain amplitudes between 0.37% and 1.0% for R ratio = −1, using the microstructural model for C263 shown in figure 1. As before, a random set of grain crystallographic orientations has been used. p_{cyc} is, of course, a field variable, but in each analysis the maximum value has been taken, as this occurs at the location where crack initiation will occur first. The plastic strain range, $\Delta\varepsilon_p$, is of course, a macro-level quantity, which is determined by taking the difference between the total applied strain (prescribed) and the elastic strain (calculated from $\Delta\sigma/E$). The results are presented in the form of a graph showing $\ln \Delta\varepsilon_p$ against $\ln p_{\text{cyc}}$. If the fatigue crack initiation criterion given in equation (3.2) is valid, then the resulting graph should be linear. The results are shown in figure 7. A trend line has been added. The results show reasonable agreement with the Manson–Coffin relationship.

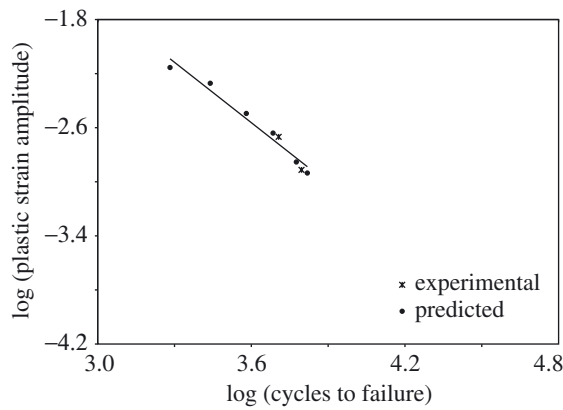


Figure 8. Comparison between experimental and predicted cycles to failure with plastic strain range for LCF at 20 °C.

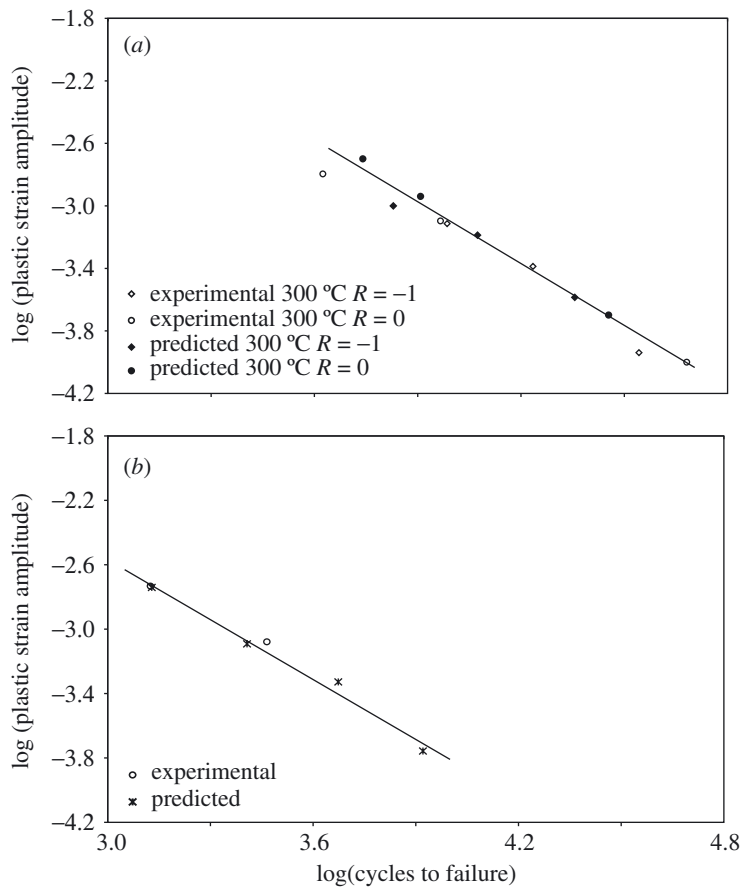


Figure 9. Predicted relationship between plastic strain amplitude and cycles to failure for LCF at (a) 300, (b) 600 °C. The linear fit is included to indicate the trend.

Two experimental LCF tests carried out at 20 °C with R ratio = -1 at strain amplitudes of 0.37 and 0.5 have been simulated (for which the hysteresis loops are shown in figure 2) using the polycrystal model. For each case, the maximum accumulated slip per cycle has been calculated, and hence, knowing the number of cycles to failure in each case (6250 and 5090 cycles respectively), the critical accumulated slip has been determined. For the two cases it was found to be 426 and 472. The average was taken, to give 449. The critical accumulated slip for nickel-base alloy C263 is therefore taken to be 449. While this dimensionless quantity seems large in magnitude, it results from the accumulation of plastic slip over many cycles. The accumulated slip per cycle is, as expected in LCF and HCF, small. We may now use the polycrystal plasticity model, together with the fatigue crack initiation criterion, to predict LCF and HCF crack initiation. We do this firstly for LCF at 20 °C, and then compare predictions with experimental data for 300 °C and 600 °C. The prediction of LCF life for the nickel alloy C263 at 20 °C for a range of strain amplitudes with R ratio = -1 is shown in figure 8. The two experimental data points are also shown. Predictions of LCF life at 300 °C, which were obtained using exactly the same critical accumulated slip, are shown in figure 9a for R ratios of -1 (with plastic strain amplitudes between 0.32 and 0.63%) and 0 (with plastic strain amplitudes between 0.29 and 0.68%). Good agreement is seen, and the model predicts the expected linear relationship between log (plastic strain amplitude) and log (cycles to failure).

At 600 °C, it was found to be necessary to re-calculate the critical accumulated slip, and it was found to be 130. A number of authors (see, for example, Stouffer & Dame 1996) have noted the possibility that in nickel alloys there exists a critical temperature below which the dominant slip process is that of octahedral slip, but above which both octahedral and cubic slip occur, the latter in just the γ' phase. For nickel alloy Rene N4, for example, the critical temperature was suggested to be *ca.* 700 °C. If it is the case that additional slip mechanisms become active in C263 at 600 °C, which seems credible (though the volume fraction of γ' in nickel alloy C263 is only *ca.* 10%), it would become likely that a lower critical accumulated slip, for octahedral slip, would then operate. However, the present model is unable to account for cubic slip. The predicted results at 600 °C are shown in figure 9b, together with the two experimental data points. Only one of the experimental points was used for the determination of the critical accumulated slip at 600 °C.

(b) HCF crack initiation

With the same critical accumulated slip of 449 used for 20 and 300 °C as for LCF above, the polycrystal plasticity model and crack initiation criterion have been used to predict the life of nickel alloy C263 under HCF conditions at 20 °C. Firstly, however, HCF is considered in a slightly more general way. The number of cycles to crack initiation in HCF has been found to be correlated well by Basquin's rule, which gives the relationship between stress range, $\Delta\sigma$, and the number of cycles to failure, N_f , as

$$\Delta\sigma N_f^b = C_2, \quad (3.7)$$

in which b and C_2 are material constants. The effect of mean stress on life in HCF is significant, and can be correlated well using Goodman's rule, which gives the relationship between the stress range, $\Delta\sigma_0$, leading to failure at N_f cycles at zero

mean stress, and that leading to the same number of cycles to failure but in the presence of a mean stress $\bar{\sigma}$. The relationship is

$$\Delta\sigma = \Delta\sigma_0 \left(1 - \frac{\bar{\sigma}}{\sigma_{TS}}\right). \quad (3.8)$$

Combining the fatigue crack initiation criterion given in (3.3) with (3.7) and (3.8) gives

$$\frac{\Delta\sigma}{1 - \bar{\sigma}\sigma_{TS}^{-1}} \left(\frac{p_{crit}}{p_{cyc}}\right)^b = C_2. \quad (3.9)$$

Because p_{crit} is a constant, this can be written as

$$\ln p_{cyc} = \ln \alpha + n \ln \left(\frac{\frac{1}{2}\Delta\sigma}{1 - \bar{\sigma}\sigma_{TS}^{-1}} \right), \quad (3.10)$$

in which α and n are constant. That is, the polycrystal plasticity model combined with the fatigue crack initiation criterion would be expected to yield a linear relationship between

$$\ln(p_{cyc}) \quad \text{and} \quad \ln \left(\frac{\frac{1}{2}\Delta\sigma}{1 - \bar{\sigma}\sigma_{TS}^{-1}} \right)$$

if they are consistent with the Basquin and Goodman HCF correlations. In order to test this, a range of stress-controlled simulations have been carried out on the model representation of the nickel alloy C263 microstructure given in figure 1. Uniaxial loading has been imposed (under plane-strain conditions) with a range of stress amplitude and mean stress. In all cases, however, the macroscopic load applied has been chosen to ensure that the macroscale stress remains linear with strain, thus producing conditions of HCF. Examination of the micro-level stress-strain behaviour, however, using the polycrystal plasticity model shows that while many of the grains are deforming purely elastically, localized regions within some grains also deform plastically, and it is in these regions that crack initiation is expected, and indeed predicted, to occur.

As before, crack initiation is assumed to occur when the maximum, localized accumulated slip achieves the value of the critical accumulated slip, namely, 449. The results of the simulations are shown by the symbols in figure 10. The stress amplitudes, mean stresses and the corresponding R ratios are also shown in the figure. For a broad range of stress amplitude and R ratios, the desired linear relationship is correctly predicted by the model for HCF. The HCF behaviour of nickel-base alloy C263 at 20 °C is investigated next.

(i) S - N curve for nickel alloy C263

As discussed above, HCF life is often correlated well using Basquin's relationship between stress amplitude and number of cycles to failure. For many materials, as the stress amplitude in HCF is reduced, a threshold stress (the fatigue limit) is achieved below which the material appears to have an infinite life. This behaviour is often shown in the form of a stress versus cycles to failure (S - N) curve. An S - N curve for nickel alloy C263 has been obtained at 20 °C using rotating-bend tests carried out on circular-section test specimens (S. Williams 2002, personal communication).

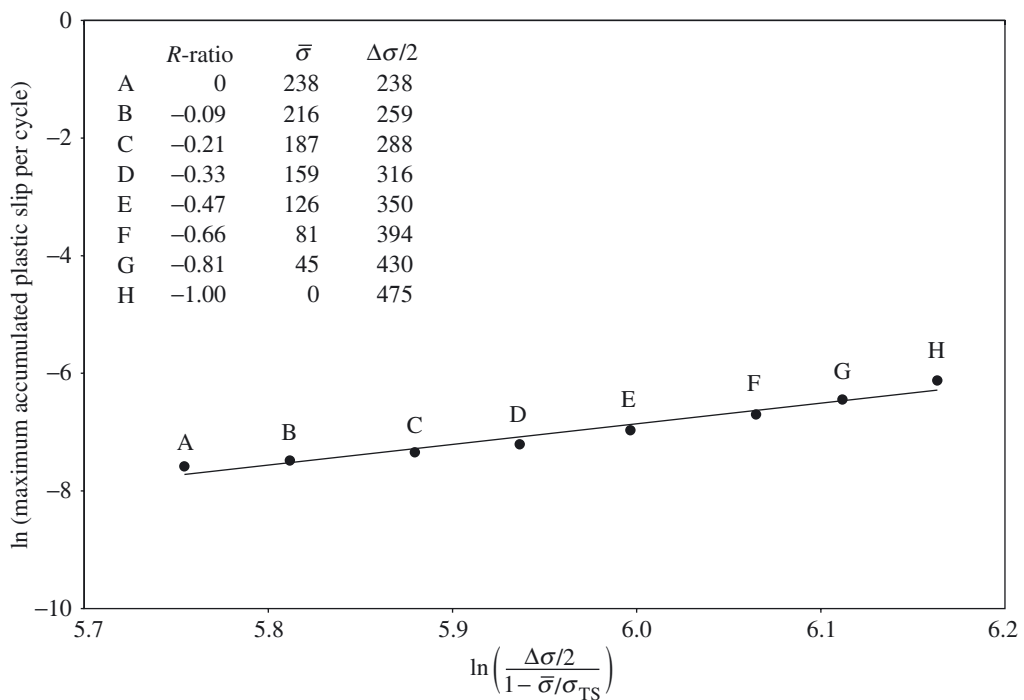


Figure 10. Predicted relationship between maximum accumulated plastic slip per cycle and stress amplitude and mean stress for HCF.

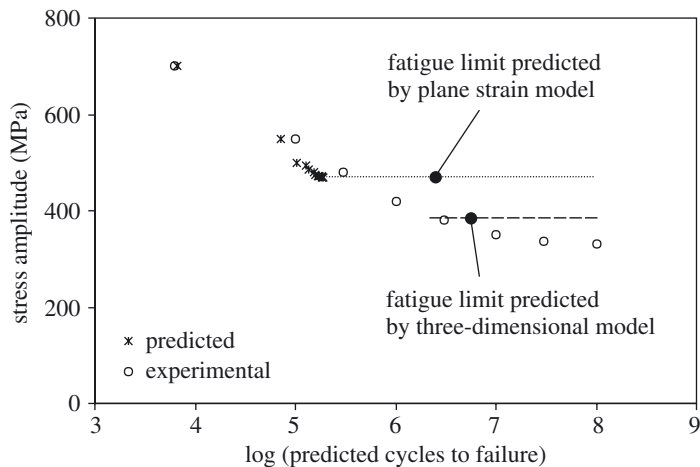


Figure 11. Predicted and experimental S - N curves at 20°C .

The results are reproduced in figure 11 and the data are shown using the circular symbols. At an experimental stress amplitude of *ca.* 350 MPa, the fatigue limit can be seen to have been reached.

The plane-strain polycrystal plasticity model with the crack initiation criterion has been used to simulate a range of HCF tests, through to crack initiation, and the predicted results are shown in figure 11 by the cross symbols. Again, note that the

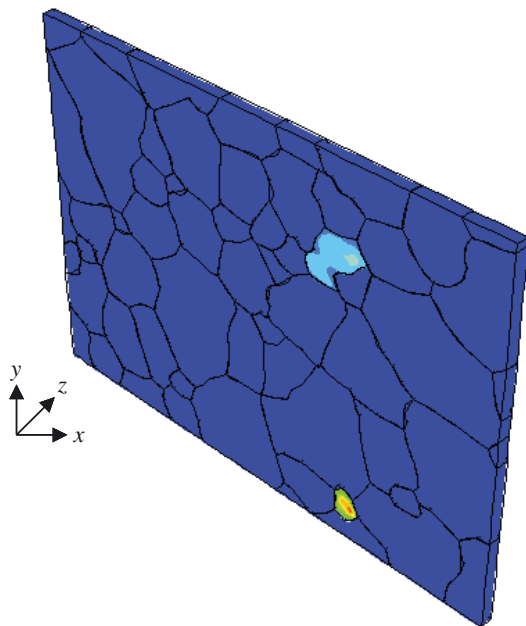


Figure 12. Three-dimensional field plot showing accumulated plastic slip after one loading cycle.

critical accumulated slip remains unchanged at 449. Good agreement can be seen between predicted and experimental results, at least at higher stress amplitude. In principle, the polycrystal plasticity model should be capable of predicting the fatigue limit (for initiation controlled failure). As the stress amplitude is reduced, ultimately, the resolved stress on the critical slip planes will fall below the critical resolved shear stress, and all the deformation, even that in the most severely loaded regions of the grains, will become elastic. At this point, there will be no further accumulation of plastic slip, and hence the critical accumulated slip will never be achieved. The model will therefore predict infinite life, and the stress range predicted for this to occur, using the plane-strain model, is shown in figure 11. In the simulations, progressively smaller stress amplitudes have been imposed, as shown in figure 11. At a stress amplitude of *ca.* 450 MPa and below, no further plastic slip is predicted to occur, so that in fact the predicted fatigue limit is *ca.* 450 MPa, as shown in the figure. As the graph shows, this is considerably higher than that seen in the experiments. It is argued that the primary reason for the overestimation of the predicted fatigue limit is the assumption made of plane strain. As is well known in fracture, the plane-strain condition imposes an additional constraint on the material, which has the effect of raising the material's effective yield stress. It is for this reason that the plastic slip ceases to occur at too high a stress amplitude in the simulations, and hence leads to an overestimated fatigue limit. In order to address this problem, a simple three-dimensional model has been developed, as shown in figure 12.

This is not a full representation of three-dimensional grains, but rather, an 'extrusion' of the two-dimensional elements into the out-of-plane direction such that prismatic grains are produced. However, three-dimensional slip systems are incorporated, the two-dimensional plane-strain constraint has been removed, and free-surfaces have

now been introduced, such that out-of-plane deformations can now occur both within grains and across them. The figure shows the accumulated plastic slip after one cycle under stress controlled HCF. The dark blue colour in the majority of the grains corresponds to a value of zero in the accumulated plastic slip, since these grains are deforming elastically. Plastic slip initiates within two grains, with a peak value, indicated by the colour red, of 1.03×10^{-5} . In both cases, the accumulated slip has been initiated, and has its peak value at or very near to grain triple points. In addition, a persistent slip band can be seen. These are the locations where crack initiation is predicted to occur.

The $S-N$ curve predictions have been repeated with the three-dimensional model. In particular, simulations with $R = 0$ loading have been carried out for a range of progressively decreasing stress amplitudes until the point when no plastic slip is initiated during a cycle. This occurs for a peak stress of 562 MPa, with a mean stress of 281 MPa. Using Goodman's rule, the stress amplitude leading to the same number of cycles to failure, for zero mean stress conditions, is 390 MPa, taking the tensile strength of C263 at room temperature as 1000 MPa. This stress is marked on figure 11, shown by one of the broken lines. The comparison of the predicted fatigue limit with the experimental points can be seen to be significantly better than that obtained with the plain strain model.

The fatigue limit calculation carried out here is on the basis that, when the stress amplitude is small enough such that no plastic slip occurs in the microstructure, even at a local level, the 'fatigue limit' has been achieved. This, of course, is an upper bound, because it is accepted that HCF crack initiation can occur in the absence of resolved shear stresses exceeding the critical value. This is a further reason why both the plane-strain and three-dimensional models over-predict the fatigue limit.

4. General application of model

The approach presented above, for initiation-controlled failure, seems capable of predicting deformation and lifetime for a broad range of HCF and LCF loading, based just on two material properties (over and above the standard elastic properties): the critical resolved shear stress and the critical accumulated slip. In order to make the predictions, however, it is necessary to develop a finite-element model which explicitly represents a small region of the material's microstructure, incorporating enough grains such that standard isotropic plasticity behaviour is captured at the macroscale. The model used here covers an area of $ca. 800 \times 500 \mu\text{m}^2$. The simulations carried out are long, typically taking 20 h to follow through two plasticity cycles. The question arises, therefore, whether such an approach is more generally applicable for structural components which almost always contain geometric stress raisers, whose length-scales are typically much larger than those possible to analyse in this way. In practice, the only feasible way of using the present approach in such applications is to use sub-modelling; that is, to use polycrystal plasticity in critical regions where crack initiation is expected, and to couple this with continuum-level modelling in other regions of the structure. At the material level, however, the approach presented has scope to be applied to investigate the effects of texture, generated through prior processing, and second-phase particles, for example, on fatigue crack initiation. Increasing computer power will continue to make this more feasible.

5. Conclusions

A polycrystal plasticity model has been developed for the nickel-base alloy C263. Using standard elastic properties together with just the critical resolved shear stress, it has been possible to predict a broad range of macroscale cyclic plasticity behaviour, for a range of temperatures, for nickel alloy C263.

A trivially simple crack initiation criterion is presented, which uses just one material property, named the critical accumulated slip. This has been determined using just two fatigue tests (though a single test would suffice). The criterion has been combined with the polycrystal plasticity model to predict a range of HCF and LCF crack initiation behaviour, and in particular, to make predictions for LCF and HCF in nickel alloy C263. The predictions for cyclic deformation and cycles to crack initiation, for a range of temperatures, are based on just two material parameters, namely, the critical resolved shear stress and the critical accumulated slip. The model predicts the development of persistent slip bands with a width of *ca.* 10 µm. Experimentally measured slip band widths in nickel single crystals have been reported to be *ca.* 10 µm (Schwab *et al.* 1996). The model also predicts that crack initiation occurs, for the aggregate of grains chosen, at grain triple points under both LCF and HCF.

The polycrystal plasticity model, with the crack initiation criterion, is able to reproduce the standard Basquin and Goodman rules for HCF crack initiation, and the Coffin–Manson relationship for initiation-controlled LCF failure. Excellent agreement for LCF life for nickel alloy C263 is achieved for a range of strain ranges and temperatures. Using a simple three-dimensional model, good agreement for HCF life is also achieved, and an upper bound for the fatigue limit for this material has been predicted.

The authors are grateful for the financial support provided by the EPSRC and thank Lygia Fielding for carrying out the three-dimensional computations.

References

- Anand, L. & Kothari, M. 1996 A computational procedure for rate-independent crystal plasticity. *J. Mech. Phys. Solids* **44**, 525–558.
- Asaro, R. J. 1983 Micromechanics of crystals and polycrystals. *Adv. Appl. Mech.* **23**, 1–115.
- Asaro, R. J. & Rice, J. R. 1977 Strain localization in ductile single crystals. *J. Mech. Phys. Solids* **25**, 309–338.
- Ballard, P., Dang Van, K., Deperrois, A. & Papadopoulos, Y. V. 1995 High cycle fatigue and finite element applications. *Fatigue Fract. Engng Mater. Struct.* **18**, 397–411.
- Chan, K. S. 2003 A microstructure-based fatigue crack initiation model. *Metall. Mater. Trans. A* **34**, 43–58.
- Dang Van, K. 1993 Macro-micro approach in high-cycle multiaxial fatigue. In *Advances in multiaxial fatigue* (ed. D. L. McDowell & R. Ellis), STP 1191, pp. 120–130. Philadelphia, PA: American Society for Testing and Materials.
- Dingli, J. P., Abdul-Latif, A. & Saanouni, K. 2000 Predictions of the complex cyclic behaviour of polycrystals using a self-consistent modelling. *Int. J. Plasticity* **16**, 411–437.
- Golub, G. H. & van Loan, C. F. 1983 *Matrix computations*. Baltimore, MA: Johns Hopkins University Press.
- Harder, J. 1999 A crystallographic model for the study of local deformation processes in polycrystals. *Int. J. Plasticity* **15**, 605–624.
- Hertzberg, R. W. 1983 *Deformation and fracture mechanics of engineering materials*. Wiley.

- Hill, R. & Rice, J. R. 1972 Constitutive analysis of elastic-plastic crystals and arbitrary strain. *J. Mech. Phys. Solids* **20**, 401–413.
- Khan, A. K. & Huang, S. 1995 *Continuum theory of plasticity*. Wiley.
- Manonukul, A., Dunne, F. P. E. & Knowles, D. 2002 Physically based model for creep in nickel-base superalloy C263 both above and below the γ' solvus. *Acta Mater.* **50**, 2917–2931.
- Manson, S. S. & Hirschberg, M. H. 1964 *Fatigue: an interdisciplinary approach*. New York: Syracuse University Press.
- Peirce, D., Asaro, R. J. & Needleman, A. 1982 An analysis of nonuniformized localized deformation in ductile single crystals. *Acta Metall.* **30**, 1087–1119.
- Peridas, G. & Hills, D. A. 2002 Crack initiation: the choice of tests available to calibrate Dang Van's criterion. *Fatigue Fract. Engng Mater. Struct.* **25**, 321–330.
- Press, W. H., Flannery, B. P., Teukolsky, S. A. & Vetterling, W. T. 1986 *Numerical recipes: the art of scientific computing*. Cambridge University Press.
- Saanouni, K. & Abdul-Latif, A. 1996 Micromechanical modelling of low cycle fatigue under complex loadings. I. Theoretical formulation. *Int. J. Plasticity* **12**, 111–1121.
- Schwab, A., Bretschneider, J., Buque, C., Blochwitz, C. & Holste, C. 1996 Application of electron channelling contrast to investigation of strain localisation effects in cyclically deformed FCC crystals. *Phil. Mag. Lett.* **74**, 449–454.
- Shepherd, D. P., Wisbey, A., Harrison, G. F., Ward, T. J. & Vermeulen, B. 2001 Cyclic operation of aero gas turbines: materials and component life implications. *Mater. High Temp.* **18**, 231–239.
- Skelton, R. P., Vilhelmsen, T. & Webster, G. A. 1998 Energy criteria and cumulative damage during fatigue crack growth. *Int. J. Fatigue* **9**, 641–649.
- Stouffer, D. C. & Dame, L. T. 1996 *Inelastic deformation of metals, models, mechanical properties and metallurgy*. Wiley.
- Strang, G. 1988 *Linear algebra and its applications*. Orlando, FL: Harcourt Brace.
- Taylor, G. I. & Elam, C. F. 1925 The plastic extension and fracture of aluminium crystals. *Proc. R. Soc. Lond. A* **108**, 28–51.
- Toth, L. S., Molinari, A. & Zouhal, N. 2000 Cyclic plasticity phenomena as predicted by polycrystal plasticity. *Mech. Mater.* **32**, 99–113.
- Wei, W., Floge, H. & Affeldt, E. E. 1991 Investigation of the low cycle fatigue behaviour of IN100 using a benchmark technique. *Scr. Metall. Mater.* **25**, 1757–1761.
- Zhang, Y. H. & Knowles, D. 2002 Internal report. Department of Materials and Metallurgy, Cambridge University, UK.